Supplementary Information for

Lithium Stripping: Anisotropic Evolution and Faceting of Pits

Revealed by *Operando* 3-D Microscopy

Adrian J. Sanchez[1], Eric Kazyak[1], Yuxin Chen[1], Jose Lasso[1], Neil P. Dasgupta[1,*]

[1] Department of Mechanical Engineering, University of Michigan, Ann Arbor, MI 48109, USA

*Corresponding Author: ndasgupt@umich.edu

S.1 Plan-View *Operando* Cell Design

The electrochemical cell implemented in this study is based on the design presented in our previous work[1]. The geometry of the cell is shown in Figure S.1 A. The design includes a disk working electrode (5 mm diameter) that is concentric with a ring counter electrode (Inner diameter 2.23 cm, Outer Diameter 1.91 cm). Optical access to the working electrode is afforded by a quartz window at the top of the cell. To a support a uniform current distribution across the working electrode surface, a vertical offset is placed between the two electrodes. COMSOL simulations of the current density distribution inside the cell are shown in Figures S.1 B-D. A uniform color is observed at the working electrode surface in Figure S.1 B and C, indicating a uniform current density distribution at the working electrode surface. The magnitude of the current density is larger at the working electrode than the counter electrode because of a smaller surface area (0.1963 cm^2 and 1.0292 cm^2). The variations in current density along the X axis of the working electrode surface are shown in Figure S.1 D where -Xo and Xo are the edges of the working electrode along the X axis. The spatial variations in current density are within 2%.

The COMSOl simulation presented in Figure S.1 was developed using the Tertiary Current module similar to our previous study.[1] To describe mass transport in the cell, the Nernst-Planck equation without convection (Eqn 1) is implemented. Furthermore, the Butler-Volmer relationship (Eqn 3) is used to describe the reaction kinetics of the electrode-electrolyte interface. The simulation also enforces electroneutrality (Eqn 3). Tables S.1 and S.2 detail the variable names and values used in the COMSOL simulation, which are from our previous study[1].

Equations

$$I = F \sum_{i=1}^{n} z_i(-D_i \nabla c_i - z_i \mu_i F c_i \nabla \phi) \tag{1}$$

$$I = I_o \left[\frac{C_{red}}{C_{bulk}} exp(\frac{\alpha F \eta}{RT}) - \frac{C_{ox}}{C_{bulk}} exp(\frac{-\alpha F \eta}{RT}) \right] \tag{3}$$

$$\sum_{i=1}^{n} z_i c_i = 0 \tag{3}$$

Table S.1 Constant/Variable Definitions

| Symbol	Definition
I_o	Exchange current density
Z_i	Net charge of species i
D_i	Diffusion coefficient of species i
C_i	Concentration of species i
F	Faraday's constant
α	Transfer coefficient
μ_i	Mobility of species i
R	Gas constant
T	Temperature
$\emptyset$	Electric Potential
C_{red}	Concentration of species to be oxidized
C_{ox}	Concentration of species to be reduced
	Concentration of species in bulk electrolyte

Table S.2 COMSOL Model Parameters

Parameter	Value	Reference
I_o	2.17 mA cm^{-2}	[1,2]
D_{Li+}	2.57 x 10^{-6} cm^2/s	[1,3,4]
D_{PF6^-}	3.96 x 10^{-6} cm^2/s	[1,3,4]
α	.5	[1,5]
T	298.75 K	
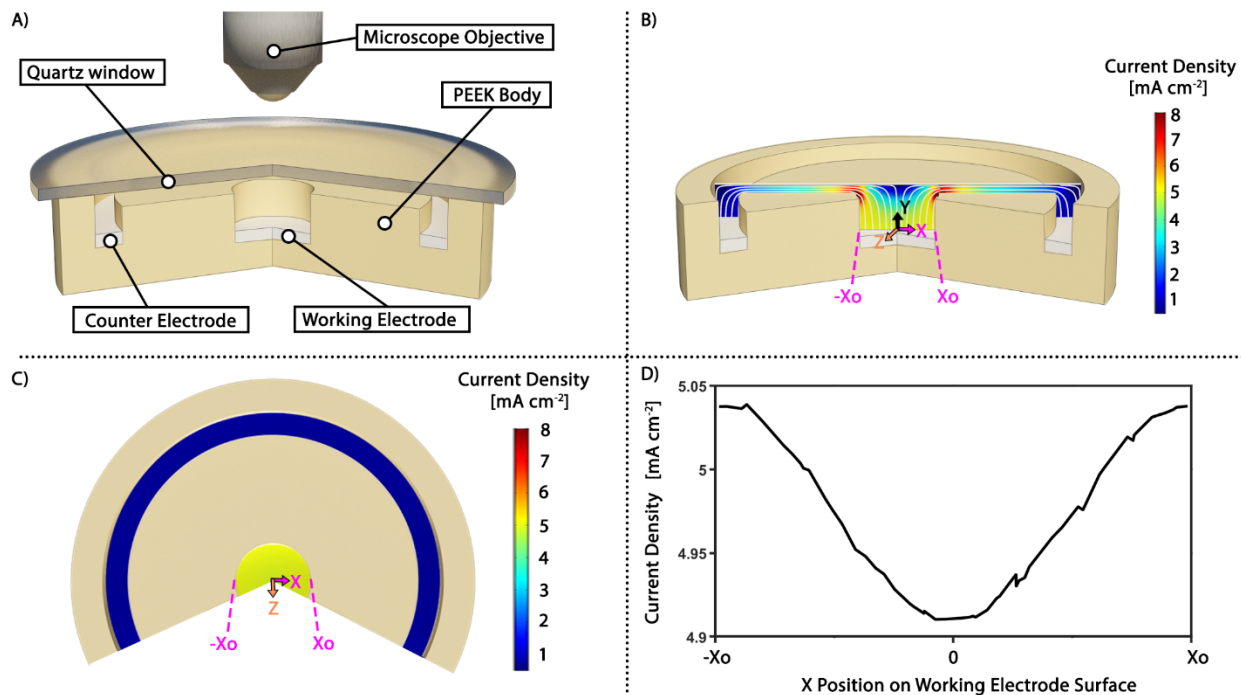
Figure S.1: a) Schematic of the plan-view cell used for *operando* analysis. b) Current density distribution within electrolyte body along a cross-section when charge is stripped from the working electrode at 5 mA cm^{-2} (area based on working electrode surface area). c) Current density at working electrode and counter electrode surface when charge is stripped from working electrode surface at same rate in c). d) Current density along working electrode surface across the X axis.

S.2 Segmentation Code

A segmentation code was developed in MATLAB® to differentiate a pit from the bulk surface. The general workflow of the script is depicted in Figure S.1. First a threshold to the luminance of the RGB image was applied to convert pixels exceeding the threshold to white and the remaining pixels to black (built-in function 'im2bw'). Second, to fill missing pockets in the pit, thresholds were applied to spatial information provided by focus variation microscopy. Pixels with a Z-coordinate below the average Z-coordinate of the bulk surface and a 3D gradient below the gradient measured at the pit edge were filled with black. Furthermore, a subsequent flood-fill operation was applied to further fill any missing pockets (built-in function 'imfill'). Third, the black regions were segmented into individual shapes, and then filtered based on area (built-in function 'bwarea'). The region with the largest area was retained, and all others were removed. Lastly, the remaining pit outline was structured with square elements (built-in function 'strel') and smoothed with a Savitsky-Golay filter with a moving average of 5 pixels. The resulting binary image highlighted with pit surface with black and the remaining regions with white.
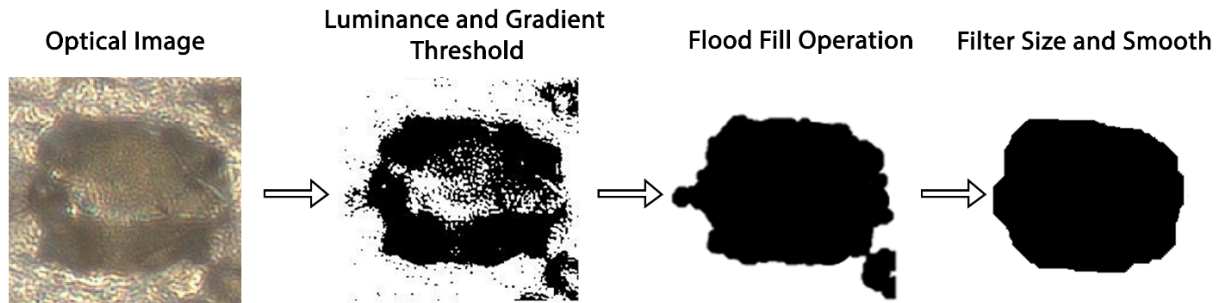
**Figure S.2:** Schematic of MATLAB segmentation code that outlines pit.

S.3 Pit Aspect Ratio Measurement

The pit aspect ratio was defined as the difference in Z-coordinate between the average bulk surface and minimum Z-coordinate within the pit. The average Z-coordinate of the bulk surface was calculated over a square border surrounding the pit as shown in Figure S.2. The dimensions of the square border that were used to compare focus variation microscopy and AFM images in Figure 2 are shown in Figure S.2 A. The width of the pit border (W) was defined as 5% of the AFM image side length (S_{AFM}). Furthermore, the outer side length of the border (S_{out}) was equated to the side length of the AFM image (S_{AFM}). The border dimensions were defined differently for Figure S.4, where AFM was not used. These dimensions are shown in Figure S.2 B. First, the averaging border was centered with the initial pit centroid (centroid during nucleation). The inner side length of the border (S_{in}) was defined by enforcing the border to be at least 2 microns away from the pit edge. To do this, the minimum distance between the inner wall of the border and the pit edge (R) was set to 2 microns. The width of the border was assigned to be 1 micron.
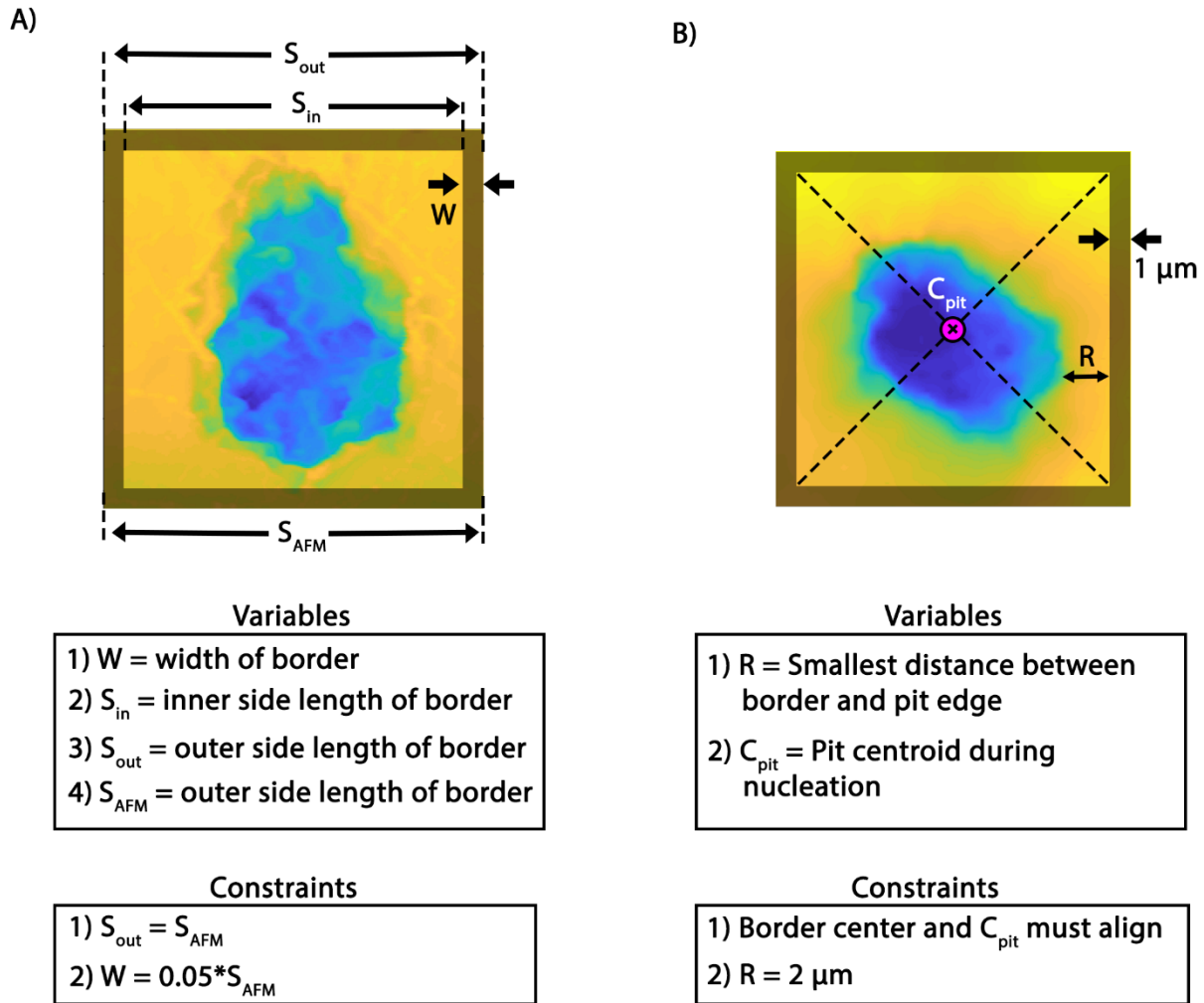

Figure S.3: a) Example AFM image with averaging border depicted. b) Example image produced with focus variation microscopy with averaging border depicted. Variables and constraints that define the border dimensions are listed.

S.4 Pit Aspect Ratio of Single Pit
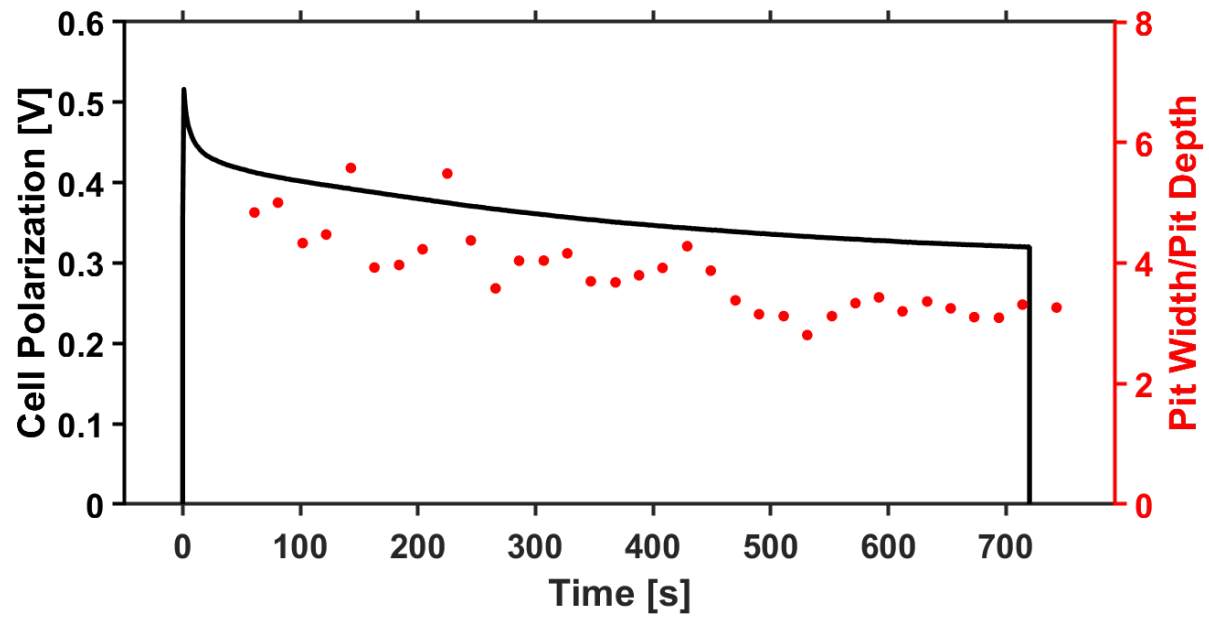
Figure S.4: Cell polarization (left axis) and the pit aspect ratio (right axis) as a function of time for pit shown in Figure 3.

S.5 Pit Aspect Ratio of Many Pits
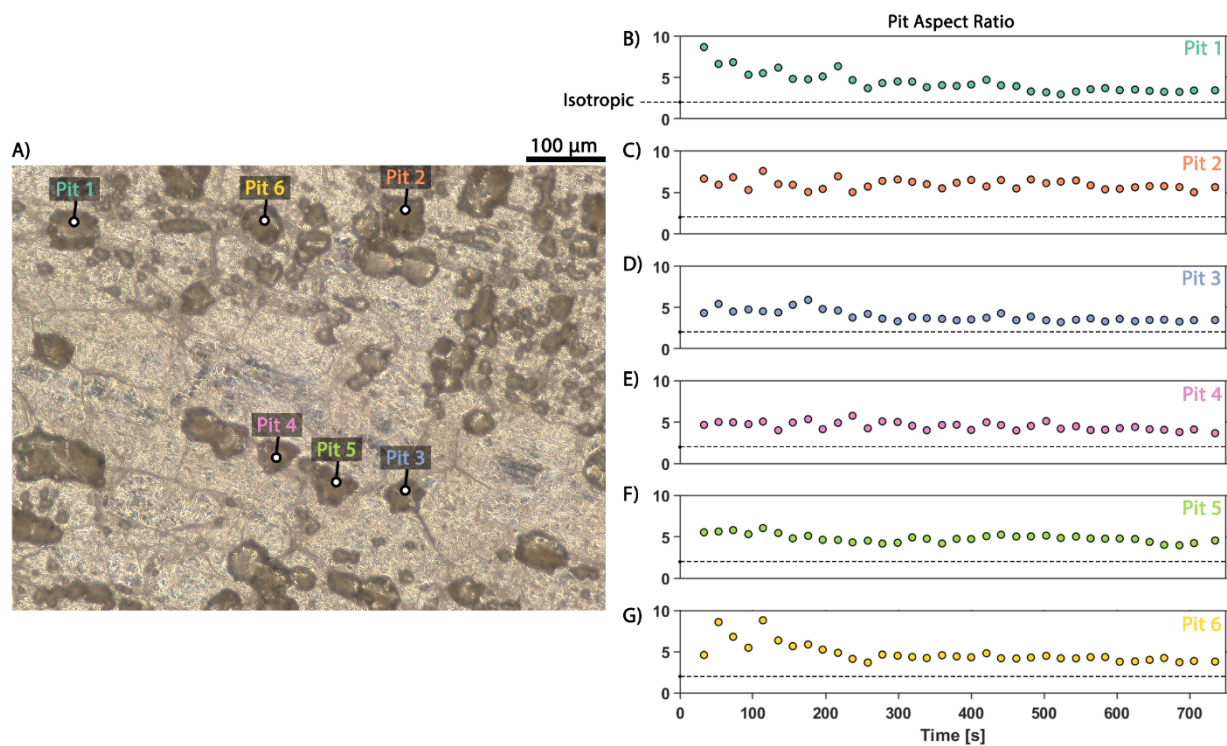
Figure S.5: a) Optical image of the working electrode from a plan-view cell after 1.1 mAh cm^{-2} of charge was stripped. b-g) Pit aspect ratio as a function of time for the pits labeled in a). Dashed line is an aspect ratio of 2, which is the expected value for isotropic expansion. Values greater than 2 indicate faster in-plane expansion.

S.6 Local Grouping of Similar Morphology
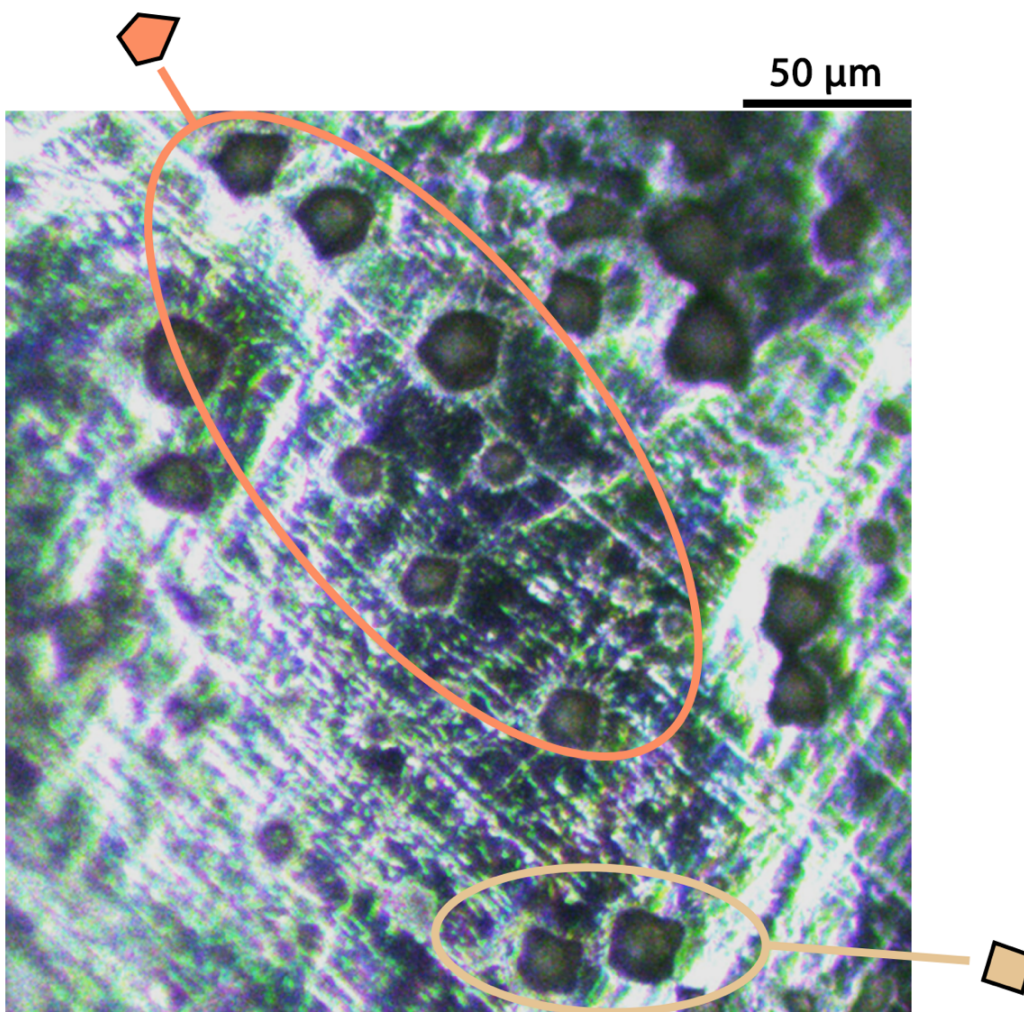
Figure S.6: Optical image of electrode surface extracted from a Li-Li symmetric coin cell after 1.1 mAh cm^{-2} of charge was stripped from the surface at 5 mA cm^{-2}. Local groupings of similar polygonal shapes were observed. The shape of each grouping varied across the electrode surface.

S.7 3-D Render Generation

3-D renders were produced by a multi-step process. First, the topographical information produced by the Keyence microscope was converted into a point cloud file in MATLAB®. Using the "Scanto3D" add-on in DS SOLIDWORKS®, the point cloud was meshed into a surface and saved as an object file. The object file was then imported in the Autodesk 3DS Max®, and the stored surface was rendered.

S.8 Further Validation of Focus Variation Microscopy – Pit Eccentricity

To further validate the focus variation microscopy technique, the eccentricity and circularity of the pits shown in Figure 1 was quantified and compared. Eccentricity is the ratio of the distance between the foci of an ellipse to the major axis length of an ellipse. Circularity is defined as $\frac{4\pi A}{P^2}$ where A and P are the shape area and perimeter respectively. These quantities are effective at capturing anisotropy since they are a measure of how circular the in-plane shape is. Both quantities are bounded between 0 and 1 where an eccentricity of 0 and circularity of 1 represent a perfect circle. Figure S.8 A shows the eccentricity and circularity of example shapes where values deviating from an eccentricity of 0 and circularity of 1 represent elongated shapes. The MATLAB function "regionprops" was utilized to fit an ellipse sand calculate eccentricity. Additionally, it was used to calculate the circularity of the pits. Figures S.8 B and C show the eccentricity and circularity values for both the AFM and focus variation microscopy. The agreement between AFM and focus variation microscopy measurements are within 3% and 12% of each other for eccentricity and circularity, respectively. This further supports that focus variation microscopy can accurately capture the anisotropic expansion of pits.
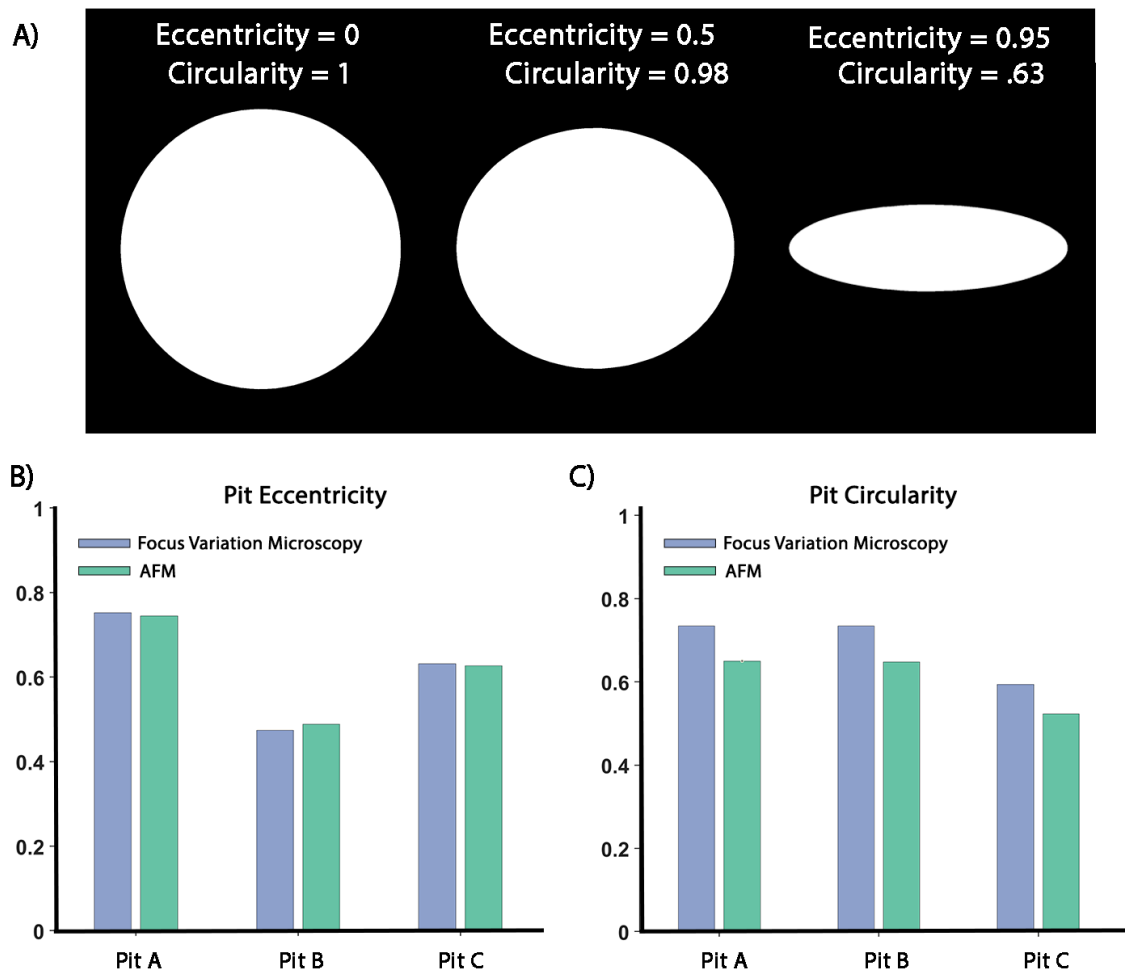
Figure S8: a) Eccentricity and circularity values of example shapes. b) Eccentricity values for Pits A, B, and C from Figure 1 of the main text. c) Circularity values for Pits A, B and C from Figure 1 of the main text.

S.9 Impact of Varying Overpotential Across Different Crystallographic Planes

As discussed in the main text, multiple factors contribute to the observed anisotropic dissolution. The expansion of the pit can be impacted by heterogeneity in the solid electrolyte interphase and by the geometric curvature of the pit. In order to isolate the influence of the difference in thermodynamic overpotential, we can hold these variables constant and calculate the impact of varying overpotential on current density with the Butler-Volmer equation:

$$i = Fk^o \left[c_{Li} \exp\left(\frac{(1-\beta)F}{RT} \eta \right) - c_{Li^+} \exp\left(-\frac{\beta F}{RT} \eta \right) \right] \tag{4}$$

where F is Faraday's constant, R is the gas constant, T is temperature, k^o is the standard heterogenous rate constant, c_{Li} is the surface concentration of metallic Li, c_{Li^+} is the surface concentration of Li ions, i is current density, β is the charge transfer symmetry coefficient, and η is overpotential.[5] In our previous study, we have developed a parameterized model of Li plating kinetics to replicate operando measurements using the same Li foils as used in this study[5]. The simulated difference in thermodynamic overpotential between the two families of planes is ~20 mV.[6] Plugging these values into Eqn 4, the resulting percent difference in current density (and thus stripping rate) is 38.7%, which would contribute to the anisotropy observed in this study.

S.10 Pit Faceting – Pentagon

Pentagonal pits were observed as shown in Figure S.11. The pentagonal shapes would not be fully explained by BCC crystal structure of Li if we were to consider a single crystal. However, many of the pits analyzed in this study (including the pit shown in Figure S. 11) span multiple grains, which is amplified by the fact that preferential pit nucleation is observed along grain boundaries. When a pit spans multiple grains at a surface grain boundary, they can combine into a pentagon. As discussed in the main text, the Li foil used in this work does not display a preferred in-plane crystallographic texture. The variations in in-plane grain orientation can thus help to rationalize the formation of pentagonal pits.

Figure S.10 A shows two hypothetical grains with different in-plane orientations. Based on the grain orientation, square pits would have formed in both grains A and B if they were isolated from the grain boundaries. However, in this example, the in-plane orientation of the two grains differs by 45°. This difference could promote a pentagonal shape if a pit were to span both grains, as illustrated in Figures S.10 B-D. When a pit nucleates at the grain boundary between grains A and B (Figure S.10 B), it will expand into both grains (Figure S.10 C). The facets that develop in each grain will be determined by its respective in-plane orientation. With the orientation depicted in Figure S.10 A, the square shapes in both grains A and B will combine into a pentagon (Figure S.10 D).
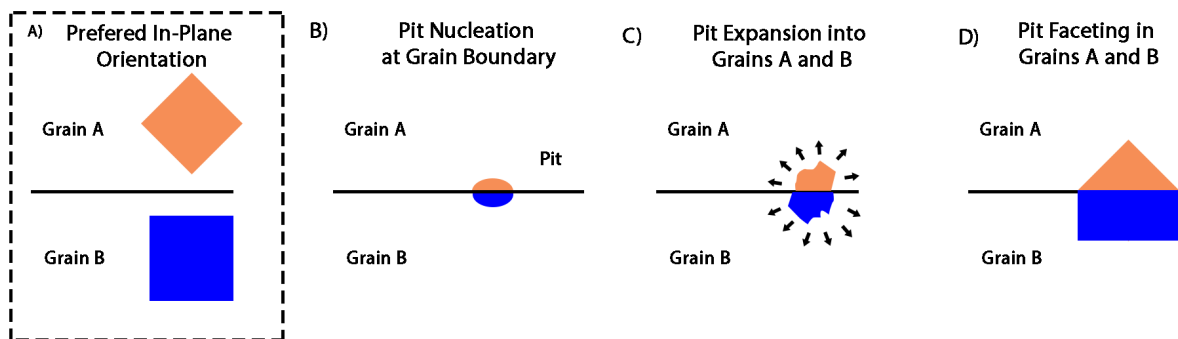
Figure S10: a) Schematic of two grains with in-plane orientation mismatch. Schematic of b) pit nucleation at a surface grain boundary, c) pit expansion into two grains with angular mismatch, and d) pit faceting in a pentagonal shape.

An experimentally observed pit with a pentagonal geometry is shown Figure S.11. The dimensions of this pit are not consistent with a regular pentagon. The internal angles of a regular pentagon would be 108°, but the measured interior angles of the pit are ~90° and ~120°. This suggest that the pit is a combination of square and hexagonal facets from adjacent grains.
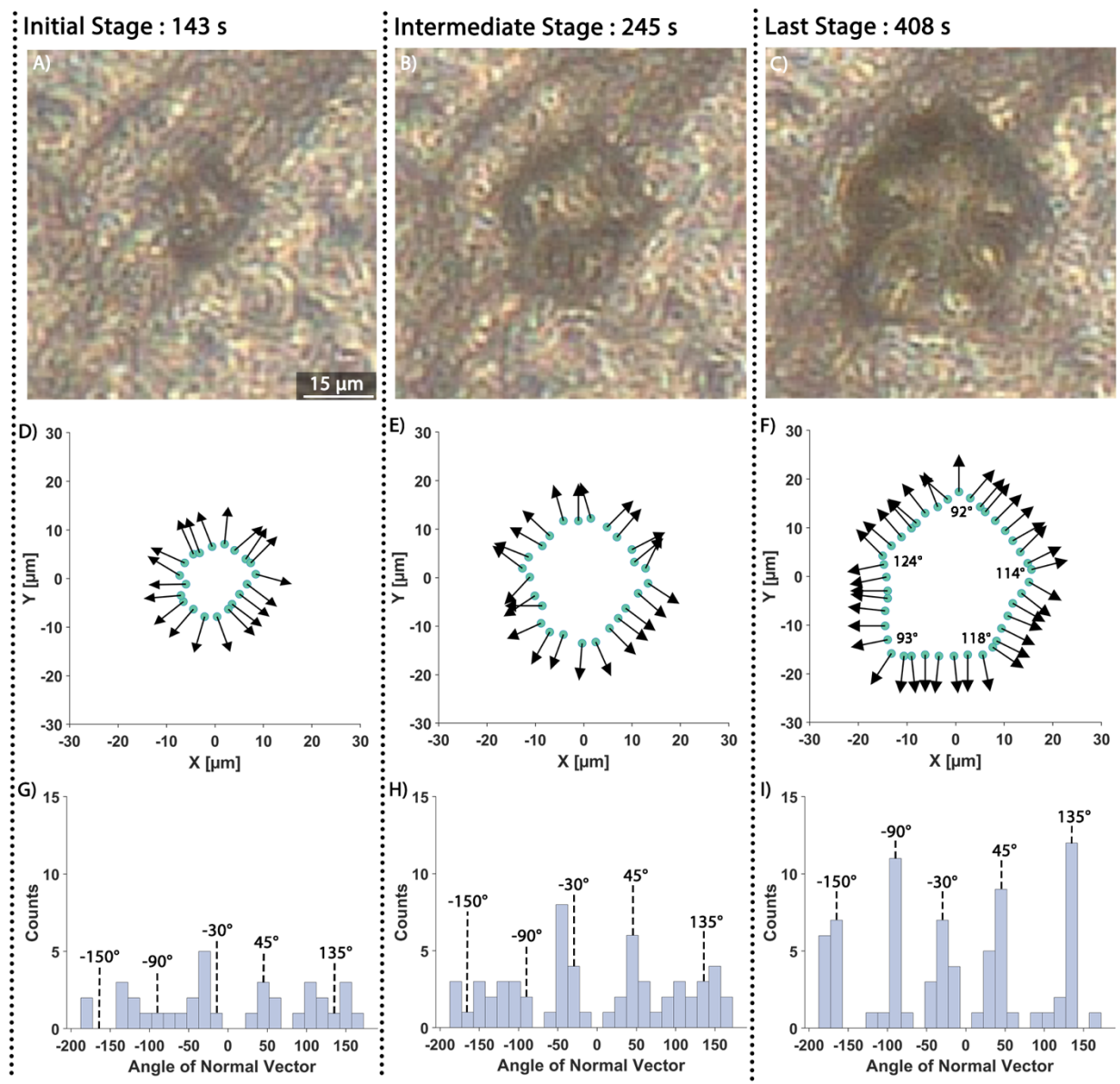
Figure S11: Optical images of a pit (A-C) captured through *operando* focus variation microscopy. Outline of pit edge and normal vectors to pit edge (D-F). Histograms of all normal vector angles with respect to the X-axis at different points in time (184 s, 286 s and 743 s respectively) during the stripping half cycle. The internal angles of the pentagon are shown in panel F.

S.11 References

1   A. J. Sanchez, E. Kazyak, Y. Chen, K. H. Chen, E. R. Pattison and N. P. Dasgupta, *ACS Energy Lett.*, 2020, **5**, 994–1004.

2   R. Tao, X. Bi, S. Li, Y. Yao, F. Wu, Q. Wang, C. Zhang and J. Lu, *ACS Appl. Mater. Interfaces*, 2017, **9**, 7003–7008.

3   Y. Saito, W. Morimura, R. Kuratani and S. Nishikawa, *J. Phys. Chem. C*, 2016, **120**, 3619–3624.

4   L. O. Valøen and J. N. Reimers, *J. Electrochem. Soc.*, 2005, **152**, A882.

5   K. N. Wood, E. Kazyak, A. F. Chadwick, K.-H. Chen, J.-G. Zhang, K. Thornton and N. P. Dasgupta, *ACS Cent. Sci.*, 2016, **2**, 790–801.

6   K. S. Nagy, S. Kazemiabnavi, K. Thornton and D. J. Siegel, *ACS Appl. Mater. Interfaces*, 2019, **11**, 7954–7964.